IEEE Access
Multidisciplinary | Rapid Review | Open Access Journal

Received May 28, 2018, accepted July 2, 2018, date of publication July 5, 2018, date of current version August 7, 2018.

*Digital Object Identifier 10.1109/ACCESS.2018.2853552*

# A W-Band Switch-Less Dicke Receiver for Millimeter-Wave Imaging in 65 nm CMOS

**GUANGYIN FENG[1], (Member, IEEE), XIANG YI[2], (Member, IEEE), FANYI MENG[3], (Member, IEEE), AND CHIRN CHYE BOON[1], (Senior Member, IEEE)**

[1]VIRTUS, IC Design Centre of Excellence, School of Electrical and Electronic Engineering, Nanyang Technological University, Singapore 639798
[2]Department of Electrical Engineering and Computer Science, Massachusetts Institute of Technology, Cambridge, MA 02139, USA
[3]School of Physical Electronics, University of Electronic Science and Technology of China, Chengdu 610054, China

Corresponding author: Xiang Yi (xiangyi@mit.edu)

This work was supported by the Singapore Ministry of Education Academic Research Fund Tier 1 under Grant MOE RG86/16.

**ABSTRACT** This paper presents a switch-less direct-detection Dicke receiver for millimeter-wave imaging applications. A configurable dual-path low-noise amplifier (CDP-LNA) with negative transformer feedback and inductive positive feedback is proposed to remove lossy switches in traditional Dicke receivers. Under a 1.8-V supply voltage, the CDP-LNA consumes 52.3-mW dc power and each path of the CDP-LNA achieves a power gain of 26.8 dB, a minimum noise figure of 6.4 dB, and a 3-dB bandwidth of 25.5 GHz. Based on the inherent switching of the CDP-LNA, a switch-less Dicke receiver is implemented, eliminating sensitivity degradation due to the insertion loss of the Dicke switch. Fabricated in the 65-nm CMOS process, the prototype exhibits a 3-dB bandwidth of 11.5 GHz with a center frequency of 82.5 GHz, achieving a noise-equivalent power of 9.3 fW/Hz0.5 and a noise-equivalent temperature difference of 0.65 K with a total power consumption of 52.6 mW.

**INDEX TERMS** CMOS, Dicke receiver, direct detection, gain boosting, low-noise amplifier (LNA), mm-wave imaging, negative-positive feedback, radiometer, transformer feedback, wideband amplifier.

## I. INTRODUCTION

Thanks to the aggressive scaling of CMOS technologies as well as promising applications of millimeter-wave (mm-wave) imaging, such as drug and explosive detection, radio astronomy, and tumor recognition, mm-wave imaging systems using CMOS platform have greatly evolved in recent years [1]–[7]. The building blocks of mm-wave imagers are similar to those used in communication systems, but mm-wave imaging receiver detects the strength of radiation or reflection to construct object images, rather than modulated signals [8], [9].

The sensitivity of mm-wave imaging systems can be expressed in terms of the minimum temperature difference that can be detected. One figure-of-merit (FoM) of imaging systems is noise equivalent temperature difference (NETD), which describes the change in temperature of a thermal source required to produce a post detection SNR of unit [3], [6], expressed as:

$$\mathrm{NETD} = T_S\sqrt{\frac{1}{B\tau} + \left(\frac{\Delta G}{G}\right)^2} \tag{1}$$

where $T_S$ is the system noise temperature, $\Delta G$ is the effective value of the imaging receiver gain fluctuations, $G$ is the overall gain of the receiver front-end, $B$ is the RF front-end bandwidth, and $\tau$ is the receiver's integration time. Therefore, as the first active stage of receiver chain, LNA with wide bandwidth and high gain will greatly improve the receiver sensitivity. For practical applications, the value of NETD is typically on the order of 0.5 K [10]. Because the temperature across a typical scene changes only a few K, too high NETD results in failing to capture usable images. Unfortunately, the fluctuations of the system's overall gain, the second item under the square root in (1), present great effects on the NETD. Imaging receivers themselves cannot distinguish between the change of radiant power and the fluctuations of RF-power-gain [3], [6].

To minimize the impact of $\Delta G$ caused by receiver instabilities, modulation principle was first introduced by Dicke [11] in 1946. The basic block diagram of traditional Dicke receivers is shown in Fig. 1. The input of LNA is periodically switched between the antenna and a reference load at a

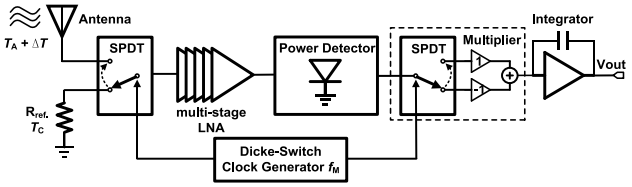


**FIGURE 1.** Diagram of traditional Dicke receivers [6].

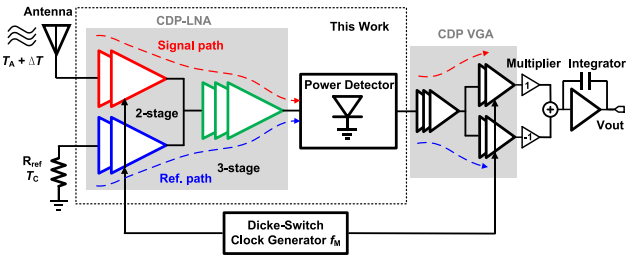


**FIGURE 2.** Block diagram of the proposed switch-less Dicke receiver.

frequency $f_M$, which is high enough in comparison with the gain variation frequencies [4]. The output voltage corresponding to reference load is subtracted from that introduced by the received signal. Thus the output voltage of the integrator is directly proportional to the signal power and modulated at the frequency $f_M$, when the noise from reference load, $T_C$, equals to that from antenna, $T_A$. The signal is received and processed by the Dicke receiver only half of the time. Therefore, the NETD is doubled compared to the total power radiometer without modulating the input signal [5], [6].

$$\text{NETD} = 2T_S\sqrt{\frac{1}{B\tau}} \tag{2}$$

The Dicke switch alleviates the receiver instabilities, but also introduces insertion loss in the RF front-end. System-level analysis indicates that 5-dB insertion loss prior to the LNA will degrade the NETD by a factor of 3 [4]. Unfortunately, the insertion loss of silicon-based mm-wave switches is quite high compared to those in III-V processes, ∼3-5 dB for CMOS switches [12], [13], which directly degrades NETD.

In order to eliminate the degradation due to the insertion loss of Dicke switch, a balanced LNA (BLNA) with four binary reflection-type phase shifters (RTPSs) was proposed in [4]. The BLNA with embedded Dicke switch uses four couplers and three five-stage LNAs. By configuring the states of RTPSs, the function of Dicke switch is achieved. The insertion loss of RTPSs comes after LNA amplification and does not degrade receiver performance as a traditional Dicke switch would. However, the mismatch between different RTPSs will introduce phase and amplitude imbalances, reducing the effectiveness of BLNA. Besides, this approach dramatically increases the power consumption and chip area due to additional LNAs and four bulky RTPSs, and thus the cost of multi-pixel imaging systems. In [14], a dual-input pseudo-switch low-noise amplifier is proposed for Dicke receiver by using two symmetric common-emitter stages driving the same common-base stage of the cascode stage. The approach eliminates the insertion loss of switches, but the isolation between two input channel is low (the simulated value is 8 dB at 100 GHz for 65nm CMOS process). Therefore, the reference noise power may be increased by input signal due to low isolation, especially when the input signal is strong. As a result, the receiver sensitivity is degraded.

In this work, a configurable dual-path LNA (CDP-LNA) is proposed for the design of direct-detection switch-less Dicke receiver for mm-wave imaging systems. This paper is organized as follows. The structure of proposed CDP-LNA-based switch-less Dicke receiver is addressed in Section II. Section III presents the circuit implementations of the proposed switch-less Dicke receiver, including the CDP-LNA, path-enable controller, and power detector. Experimental results of proposed CDP-LNA and Dicke receiver are demonstrated in Section IV. Finally, a summary of the results and concluding remarks are provided in Section V.

## II. PROPOSED SWITCH-LESS DICKE RECEIVER

Fig. 2 shows the block diagram of CDP-LNA-based direct-detection Dicke receiver. The proposed CDP-LNA consists of one signal path connected to an antenna and one reference path connected to a reference load. Either path of the proposed CDP-LNA is a five-stage LNA separated into two parts, namely, configurable stages (in red and blue) and shared stages (in green). The transistor gates of configurable stages are controlled by a clock signal, which is high enough in comparison with gain variation frequencies. When the signal path is enabled (high bias voltage), the received signal from antenna is detected by power detector and processed by following blocks, and the noise from reference load is isolated because the first two stages of reference path are disabled (low bias voltage). Likewise, when the reference path is enabled, only the noise power from reference load is detected by power detector, and received signal from antenna is isolated. The same design method can be adopted by the variable gain amplifier (VGA), which is used to amplify the output signal of power detector. Therefore, the function of Dicke switch is realized without any lossy switches at the input port of LNA. The output voltage of the integrator is directly proportional to the difference between output voltages corresponding to reference load and that introduced by received signals.

Note that the proposed CDP-LNA uses first two stages as configurable stages and the following three stages as shared stages. In this case, simulated isolation between two input ports is higher than 60 dB, which is high enough to prevent strong signals overwhelming the noise from reference load. Otherwise, receiver sensitivity will be degraded by the leakage [11]. Instead of using the proposed CDP-LNA, two separate LNAs without shared stages could be used for signal path and reference path, respectively. However, there are two main drawbacks for this topology. Firstly, the process and mismatch variations between two separate LNAs will affect the NETD of Dicke receiver. Ideally, the gains for signal path

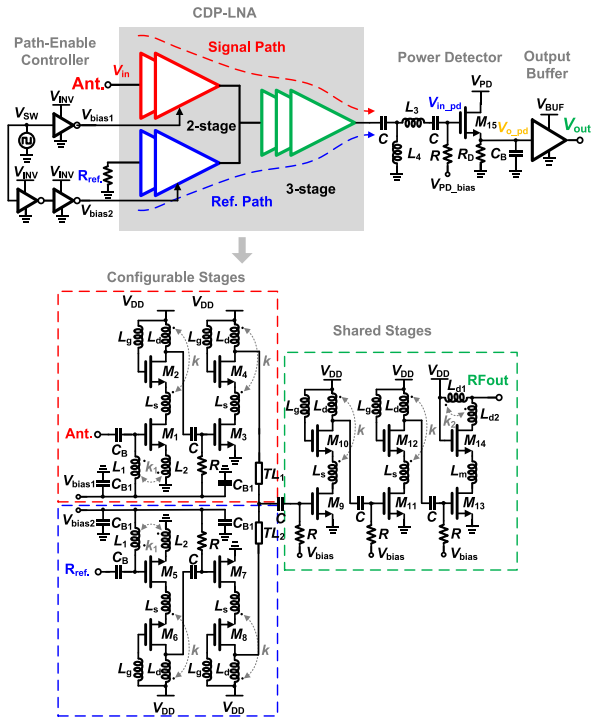


**FIGURE 3.** Schematic of the proposed CDP-LNA-based switch-less direct-detection Dicke receiver.

and reference path should be identical [11]. Secondly, two separate LNAs occupy larger silicon size, leading to higher fabrication cost. The circuit implementation of CDP-LNA will be fully described in the next section.

## III. CIRCUIT IMPLEMENTATION

Fig. 3 shows the implementation of the CDP-LNA-based switch-less direct-detection Dicke receiver, which consists of a configurable dual-path LNA with a path-enable controller, a power detector, and an output buffer. One input port of the CDP-LNA is used to receive RF signal from antenna, while the other input port is connected to a reference load resistor (50 Ω). The output port of the CDP-LNA is directly connected to the power detector. An output buffer with unity gain is utilized to drive the large load capacitor of testing equipment.

Different from traditional Dicke receivers, the CDP-LNA-based switch-less Dicke receiver removes high loss SPDT switches. Through the path-enable controller of the CDP-LNA, the input signal and reference load are switched periodically without degrading the receiver's NETD. In addition to the elimination of Dicke switch in the proposed Dicke receiver, the isolation between two input ports is also significantly enhanced due to the high isolation of cascode amplifiers.

### A. CDP-LNA

The CDP-LNA consists of two parts, switchable stages and shared stages, and each stage is a cascode amplifier. Compared to common-source (CS) or common-gate (CG)

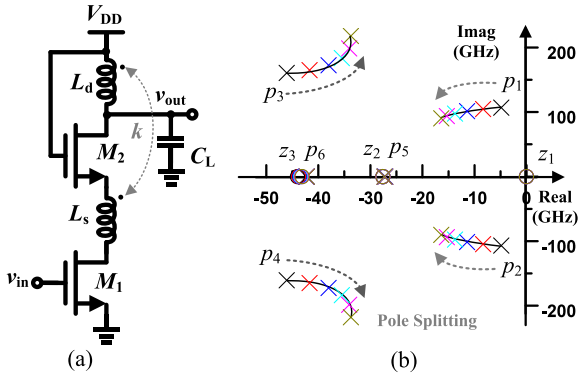


**FIGURE 4.** (a) Implementation of negative transformer feedback in a cascade LNA, (b) Pole splitting as the k increases from 0 to 0.5.

topologies, cascode LNAs exhibit better isolation, improved bandwidth and higher gain even at mm-wave frequencies, which can also be simultaneously noise and input-impedance matched [15]. As the first active stage of imaging receiver chain, LNA with wide bandwidth and high gain will significantly reduce NETD, improving image resolution. However, at millimeter-wave frequencies, the conventional single-stage amplifier exhibits relatively low gain because of operating near the cut-off frequency $f_T$ of the transistor. Moreover, the device parasitic effects and passive losses are also increasing with the operating frequency. Although the overall gain and bandwidth can be enhanced by increasing the number of stages and bandwidth can be improved though gain steering technique [16], the total power consumption will also be greatly increased. To overcome these limitations, negative and positive feedback technique is proposed for wide bandwidth and high gain. The negative feedback is to achieve wide bandwidth, while the positive feedback is to enhance power gain.

#### 1) NEGATIVE TRANSFORMER FEEDBACK

At mm-wave frequencies, parasitic capacitances have significant effects on the transistor characteristics, leading to lower gain and narrower bandwidth. Inductive load, $L_d$, is used to cancel the parasitic capacitance at frequencies of interest for maximum gain. A series inductor, $L_s$, is placed between the CS and CG transistors to tune out the middle pole of the cascode and compensate for its lower $f_T$ [15]. By magnetically coupling $L_d$ and $L_s$, forming a negative transformer feedback, the bandwidth of the cascode LNA is extended due to pole splitting, as demonstrated in Fig. 4.

Fig. 4(b) shows the simulated pole splitting in s-plane. As $p_5$ ($p_6$) and $z_2$ ($z_3$) are close enough, their effects on frequency response are cancelled with each other. When there is no coupling between $L_d$ and $L_s$, the frequency response is dominated by p1 and p2 because they are much closer to the imaginary axis [17], [18]. As the increasing of coupling efficient, the real parts of $p_3$ and $p_4$, the distance to imaginary axis, are reduced. Therefore, their effects on the frequency response become comparable with those from $p_1$ and $p_2$. Besides, the imaginary parts of $p_3$ and $p_4$ moves away from

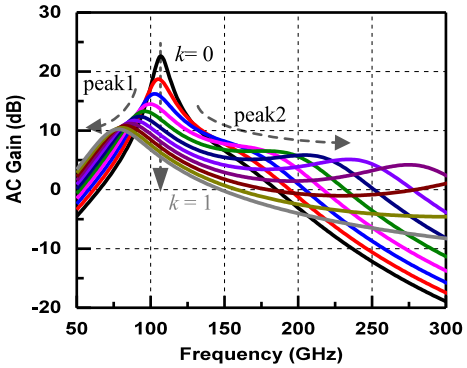


**FIGURE 5.** Simulated frequency response as k increases from 0 to 1.

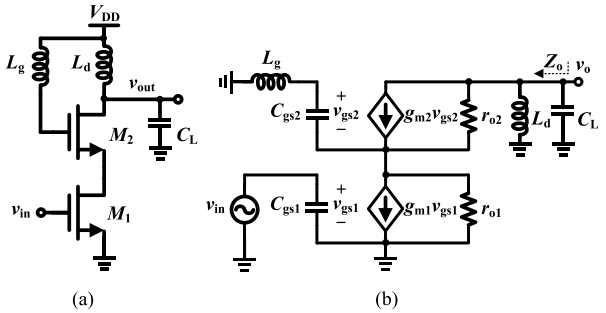


**FIGURE 6.** (a) Implementation of inductive positive feedback in a cascade LNA, (b) simplified small-signal equivalent circuit.

the origin, pushing to higher frequency, while the imaginary parts of $p_1$ and $p_2$ moves towards the origin, pulling to lower frequency. As a result, the bandwidth of the cascode LNA is enhanced by the drain-source-transformer negative feedback.

To gain more intuitional understanding about the effects from the negative feedback, simulated frequency responses versus the strength of negative feedback are demonstrated in Fig. 5. As the coupling efficient increases from 0 to 1, the frequency response exhibits two peaks which are introduced by the two conjugate pole pairs, respectively.

The second peak moves fast towards higher frequency, while the first peak moves slowly to lower frequency, leading to wider bandwidth. Although the bandwidth is extended a lot due to the pole splitting, ripples of frequency response between two peaks also becomes much more severe. Besides, the peak value of frequency response decreases a lot compared to the one without negative feedback, especially the second peak value, which decreases much faster than the first one. In order to obtain a flat frequency response over wide bandwidth, the value of second peak needs to be enhanced, which is higher than 10 dB.

### 2) INDUCTIVE POSITIVE FEEDBACK

At millimeter-wave frequencies, the conventional single-stage amplifier exhibits relatively low gain and parasitic effects and passive losses also increase with the operating frequency. Although the overall gain can be enhanced by increasing the number of stages, the power consumption will also increase greatly. Therefore, Gm-boosting techniques are developed to improve the gain of each single stage.

The basic operation principle of Gm-boosting technique is to increase the voltage swing, vgs, between the gate and source of transistor in either active or passive way. Since the active implementation introduces additional noise and consumes more power, the passive method is more attractive for realization of $G_m$-boosted LNA. There are several kinds of passive implementation in literature, such as transformer-coupled $G_m$-boosting [19], capacitor cross-coupling (CCC) [20], and gate inductor feedback [21]. The transformer-coupled $G_m$-boosting technique provides anti-phase operation between gate inductor and source inductor, leading to the increase of $v_{gs}$. However, it is limited by the turn ratio of the transformer, which is usually less than three at millimeter-wave frequencies. The capacitive cross-coupling is passive amplification and very suitable for differential LNAs. The amplification depends on the divider between the cross-coupled capacitor and gate-source parasitic capacitor, and its value is lower than one [19]. On the contrary, the $G_m$ boosting of gate inductor positive feedback can be very large, which is dependent on the value of the gate inductor.

Fig. 6 shows a cascode LNA with inductive positive feedback. Instead of connecting to the bias voltage directly, the gate terminal of $M_2$ is biased through a gate inductor$L_g$. Fig. 6(b) illustrates the equivalent circuit of the cascode LNA with inductive positive feedback. Because of the $L_g$, the gate terminal of $M_2$ is no longer a perfect ac ground. Based on the small signal analysis, the voltage drop on the intrinsic capacitor $C_{gs2}$ and real part of output impedance are expressed as (3) and (4), respectively. Since $\omega_0$ is much larger than the frequency of interest and inversely proportional to the value of $L_g$, $v_{gs2}$ and $Z_o$ increase with the gate inductor. Thus a positive feedback is introduced by the gate inductor, which results in the gain boosting of the cascode LNA. However, the value of $L_g$ is larger than $1/\omega^2 C_{gs2}$, the real part of output impedance will become negative, leading to stability issue.

$$v_{gs2}(\omega) = \frac{g_{m1} r_{o1} \left(r_{o2} + R_p\right) v_{in}}{\left(1 - \frac{\omega^2}{\omega_0^2}\right) R + g_{m2} r_{o1} r_{o2} + j\omega \left(r_{o2} + R_p\right) r_{o1} C_{gs2}} \tag{3}$$

$$Re[Z_o] = r_{o2} + \frac{r_{o1}\left(g_{m2} r_{o2} + 1\right)\left(1 - \frac{\omega^2}{\omega_0^2}\right)}{\left(1 - \frac{\omega^2}{\omega_0^2}\right)^2 + \left(\omega C_{gs2}\right)^2} \approx \frac{g_{m2} r_{o1} r_{o2}}{1 - \frac{\omega^2}{\omega_0^2}} \tag{4}$$

where $\omega_0 = 1/\sqrt{L_g C_{gs2}}$, $R = r_{o1} + r_{o2} + R_p$, and $R_p$ is the equivalent parallel resistance at the resonant frequency of $L_d$ and $C_L$.

Fig. 7(a) shows the cascode LNA with negative transformer feedback and inductive positive feedback. Thanks to the $G_m$-boosting of the positive feedback, gain reducing due to the negative feedback can be compensated. Fig. 7(b) demonstrates the simulated frequency response as $L_g$ increases from 0 to 100 pH when the coupling coefficient of transformer

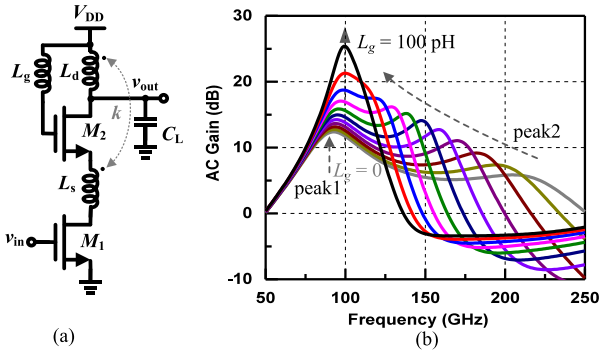


**FIGURE 7.** (a) Schematic of a cascode LNA with negative transformer feedback and inductive positive feedback, (b) simulated frequency response as $L_g$ increases from 0 to 100 pH when k = 0.5.

feedback is 0.5. With the increasing of gate inductor, both the two peak values of frequency response are increased, and the second peak is enhanced a lot compared to that without inductive positive feedback. Besides, the frequency of first peak is almost fixed, while the frequency of second peak moves towards the first one. As a result, the ripple between two peaks is greatly reduced, leading to a flat frequency response. In a word, by optimizing the negative transformer feedback and inductive positive feedback, a flat frequency response over a wide bandwidth can be achieved.

### B. PATH-ENABLE CONTROLLER

The configurable stages are composed of two identical branches controlled by a path-enable controller, as shown in Fig. 3. The two branches are biased through inverters with opposite phase operation, and the control clock is provided by an external signal generator, which can be replaced by an on-chip ring oscillator. When $V_{sw}$ is low, the upper path is enabled, otherwise, the under path is activated. When either path is enabled, the corresponding bias voltage is set to high and equals to $V_{INV}$. By changing the value of $V_{INV}$, various biasing voltage for the first two stages can be obtained.

### C. POWER DETECTOR

In the direct-detection receiver, a power detector is used to convert the input RF power to an output DC voltage. The power detector should operate in the square-law region; therefore, the input power and output voltage have a linear relationship [4]. A short-channel transistor has a very linear $I$-$V$ characteristic; nevertheless, it can generate relatively large second order harmonics by proper biasing [3]. Thus, the responsivity of power detector can be improved with optimal bias. As shown in Fig. 3, the power detector consists of $M_{15}$ and $R_D$ with $L_3$ and $L_4$ forming the input matching network.

Fig. 8 shows the transient simulation results of the Dicke receiver under an 80-GHz input signal with power level of −40 dBm. The frequency of control signal is 100 KHz. When Vbias1 is high, the signal path is enabled. The received weak RF signal is amplified and detected by the power detector, while the noise from reference load is isolated, and vice versa.

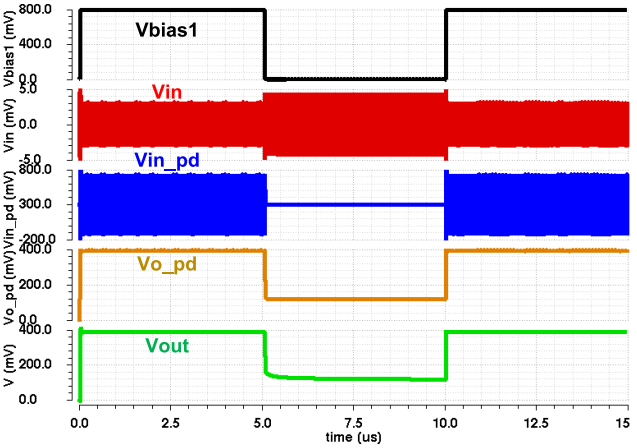


**FIGURE 8.** Simulated waveforms of the Dicke receiver under an 80-GHz input signal with power level of -40 dBm (node names labelled in Fig. 3).

**TABLE 1.** Design parameters in the switch-less dicke receiver.

| @80GHz | $L_1$ | $L_2$ | $L_3$ | $L_4$ | $L_g$ | $L_s$ | $L_d$ | $L_{d1}$ | $L_{d2}$ |
|---|---|---|---|---|---|---|---|---|---|
| Ind. (pH) | 45 | 27 | 42 | 120 | 71 | 88 | 55 | 39 | 63 |
| Q | 10.3 | 13.7 | 13.1 | 11.9 | 13.3 | 15.1 | 9.6 | 12.6 | 13.2 |
| | $k$ | $k_1$ | $k_2$ | $R$ | $R_D$ | $C$ | $C_B$ | $C_{B1}$ | $M_1$-$M_{15}$ |
| | 0.43 | 0.41 | 0.31 | 17 kΩ | 20 kΩ | 176 *f*F | 200 *f*F | 1.0 pF | 25 μm |

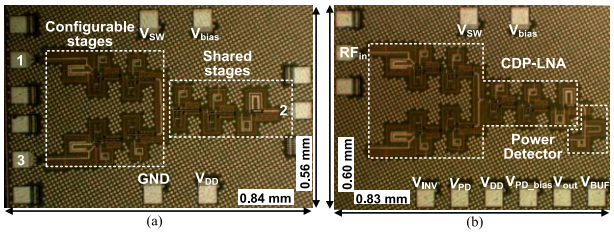


**FIGURE 9.** (a) Die micrograph of the standalone CDP-LNA, (b) Die micrograph of the CDP-LNA-based switch-less direct-detection Dicke receiver.

Design parameters of the CDP-LNA based switch-less Dicke receiver is listed in Table 1. Transformers, inductors, and all the interconnects are simulated using 3D EM simulator ANSYS HFSS since parasitics affect the performance a lot at mm-wave frequencies. Two top metals with thickness of 3.3 $\mu$m and 1.325 $\mu$m are stacked for the primary and secondary windings, respectively, to obtain high coupling factor and high quality factor.

## IV. EXPERIMENTAL RESULTS

The CDP-LNA-based switch-less Dicke receiver was fabricated in GlobalFoundries 65 nm CMOS technology. Fig. 9 shows the die micrographs of the standalone CDP-LNA and the switch-less Dicke receiver with silicon sizes of 0.47 mm$^2$

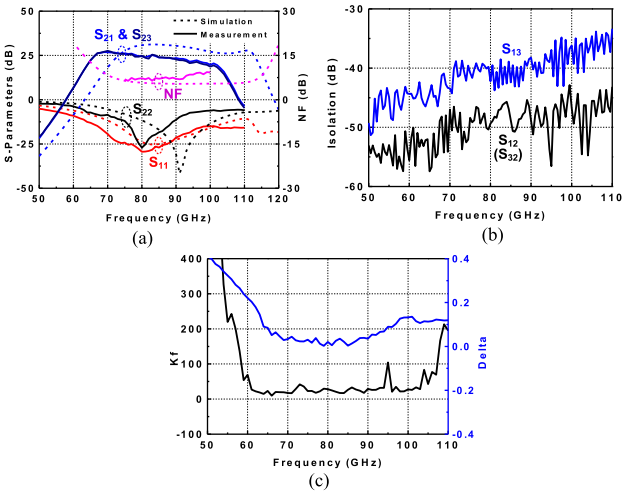


**FIGURE 10.** (a) Measured S-parameters and NF of the CDP-LNA, (b) Measured isolation of the CDP-LNA. (c) Measured stability factors K and Δ.

and 0.50 mm$^2$, respectively, including all the pads. Under a supply voltage of 1.8 V, the LNA presents a power consumption of 52.3 mW, while the power detector and output buffer consume 0.3 mW dc power.

### A. CDP-LNA

The CDP-LNA was measured from 50 GHz to 110 GHz through on-wafer testing. Fig. 10(a) depicts the measured S-parameters and noise figure (NF) of CDP-LNA. The CDP-LNA achieves a peak gain of 26.8 dB at 70 GHz and 3-dB bandwidth of 25.5 GHz, which is from 65.5 GHz to 91 GHz. The power gains of two paths ($S_{21}$ and $S_{23}$) show good agreement with each other. Within the 3-dB bandwidth, the output return loss is higher than 8 dB, while the input return loss is higher than 13 dB. Compared to the simulated result, the frequency response shifts down ∼10 GHz and the 3-dB bandwidth is reduced by ∼11.5 GHz. It is mainly due to parasitic capacitances caused by dummy metal fills which affect the performance of inductors and transformers and were not fully considered in the EM simulation because of limited computation resource. NF was measured from 75 GHz to 100 GHz, and the minimum NF is 6.4 dB at 83 GHz with an average value of 7.1 dB. The $S_{12}$ ($S_{32}$) is the reversion isolation and is better than 45 dB in the frequencies of interest, as shown in Fig. 10(b). Higher reversion isolation means better stability. The isolation between the two input ports, $S_{13}$, is higher than 35 dB. Compared to the isolation of CMOS SPDT [12], that of the CDP-LNA exhibits more than 15 dB improvement because of the high isolation of cascode topology. Fig. 10(c) shows the Rollett's stability factors $K$ and Δ, which are calculated based on the measured S-parameters, indicating the stability of CDP-LNA.

Table 2 lists performance summary of the CDP-LNA and comparisons with wideband mm-wave LNAs in CMOS. As can be seen, the proposed negative transformer feedback and inductive positive feedback extend the bandwidth of cascode LNA with high figure-of-merit.

**TABLE 2.** Performance summary of the CDP-LNA and comparisons with wideband MM-wave LNAs in CMOS.

| Ref. | Tech. | Top. | Gain (dB) | BW* (GHz) | NF (dB) | Power (mW) | FoM |
|---|---|---|---|---|---|---|---|
| [3] | 65-nm CMOS | 3-stage cascode | 15 | 12 | 7.0 | 42 | 0.4 |
| [6] | 65-nm CMOS | 5-stage cascode | 14 | 23 | 4.8 | 32 | 1.8 |
| | | | 27 | 13.5# | 6.8 | 36 | 2.2 |
| [16] | 65-nm CMOS | 5-stage cascode | 16.7 | 21.5 | 7.2 | 48.6 | 0.7 |
| [18] | 65-nm CMOS | 3-stage cascode | 18.5 | 30 | 5.5 | 27 | 3.6 |
| [22] | 45-nm CMOS | 3-stage CS | 10.7 | 18 | 6.0 | 52 | 0.4 |
| [23] | 28-nm CMOS | 2-stage cascode | 13.8 | 18 | 4.0 | 24 | 2.4 |
| [24] | 65-nm CMOS | 4-stage CS | 14.8 | 21 | 7.5 | 86 | 0.3 |
| **This Work** | **65-nm CMOS** | **5-stage cascode** | **26.8** | **25.5** | **6.4** | **52.3** | **3.2** |

* 3-dB bandwidth; # estimated value from figures;

$$\text{FoM} = \frac{Gain[\text{abs.}] \times BW[\text{GHz}]}{(F-1) \times P_{DC}[\text{mW}]}$$

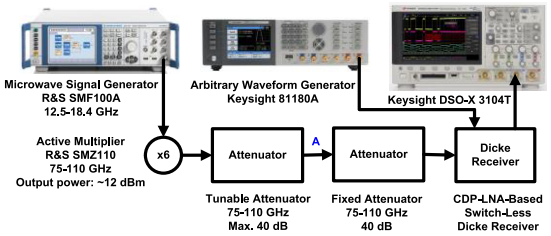


**FIGURE 11.** Measurement setup of the switch-less Dicke receiver.

### B. SWITCH-LESS DICKE RECEIVER

Fig. 11 illustrates the measurement setup of the CDP-LNA based switch-less Dicke receiver. A W-band signal source chain is used to generate different RF signals, which consists of a microwave signal generator, a W-band multiplier, a fixed 40-dB attenuator, and a tunable attenuator. Before testing the Dicke receiver, node A was directly connected to a W-band power meter to measure the input power level. Different power levels are achieved by adjusting the tunable attenuator, while different frequencies of input signal are obtained by changing the output frequencies of signal generator. The Dicke switch clock is provided by an external arbitrary waveform generator. The output voltages corresponding to the injected power and reference load are measured by an oscilloscope, as shown in Fig. 12. The voltage difference Δ Vout is calculated by subtracting the output voltage corresponding to reference load from that introduced by the injected signal.

Fig. 13 shows the Δ Vout of the Dicke receiver under input RF signal with different power levels and frequencies, respectively. The ratio between Δ Vout and input power level is defined as receiver's responsivity. To obtain the input power sensitivity and responsivity of the Dicke receiver,

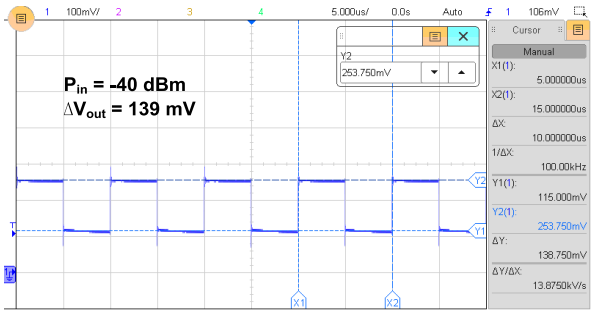


**FIGURE 12.** Measured output waveform of the Dicke receiver under an 80-GHz input signal with power level of -40 dBm.

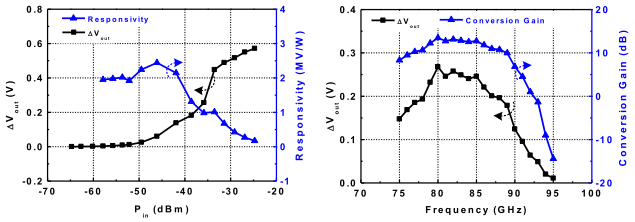


(a) (b)

**FIGURE 13.** (a) Measured$\Delta$ Vout and corresponding responsivity versus input power at 80 GHz; (b) Measured $\Delta$ Vout and corresponding conversion gain versus input signal frequency with power level of -40 dBm.

the power level of an 80-GHz input RF signal is swept from –25 dBm to –65 dBm under a control clock of 100 KHz. The receiver achieves sensitivity of –60 dBm and peak responsivity of 2.5 MV/W, as shown in Fig. 13(a). To characterize the receiver bandwidth, an input RF signal with power level of -40 dBm is injected and the frequency is swept from 75 GHz to 95 GHz. The output voltage is recorded by the oscilloscope, and the conversion gain (CG) is calculated from (5). The receiver exhibits 3-dB bandwidth of 11.5 GHz and peak conversion gain of 12 dB, as shown in Fig. 13(b)

$$\mathrm{CG(dB)} = 10\log\left(V_{out}^2 \Big/ 50\right) - P_{in} \tag{5}$$

Another figure-of-merit (FoM) of imaging systems is noise-equivalent power (NEP), which is defined as the inputsignal power that gives a signal-to-noise ratio (SNR) of unit in one hertz output bandwidth. Smaller NEP corresponds to a more sensitive receiver. According the definitions, the NEP and NETD of Dicke receiver can be derived as (6) and (8), respectively [7].

$$\mathrm{NEP} = \frac{V_n \Big/ \sqrt{B}}{V_{out} \Big/ S} = \frac{S}{\sqrt{B}} \tag{6}$$

$$\mathrm{F} = \frac{\mathrm{SNR}_{in}}{\mathrm{SNR}_{out}} = \frac{S \Big/ KT_0B}{V_{out}^2 \Big/ V_n^2} = \frac{S}{KT_0B} \tag{7}$$

$$\mathrm{NETD} = \frac{2T_S}{\sqrt{B\tau}} = \frac{2T_0 \cdot (F-1)}{\sqrt{B\tau}} \tag{8}$$

where $V_{\mathrm{out}}$ is output voltage, $V_{\mathrm{n}}$ is output noise, K is the Boltzmann constant ($\mathrm{K} = 1.38\times10^{-23}$ J/K), $S$ is the injection power at the sensitivity level which results in $\mathrm{SNR}_{\mathrm{out}}$ of unit($V_{\mathrm{out}}$ equals to $V_{\mathrm{n}}$), $B$ is the receiver bandwidth, $T_{\mathrm{S}}$ is the system noise temperature in Kelvin, $T_0$ is the room noise temperature (290 K), and $\tau$ is the integration time (typically 30 ms) [7].

Calculated from (6)– (8), the NEP, NF, and NETD of the designed switch-less Dicke receiver are 9.3 $f$W/Hz$^{0.5}$, 13 dB, and 0.65 K, respectively. The measured peak responsivity is 2.5 MV/W, which can be further enhanced by a baseband amplifier. Performance of the implemented CDP-LNA-based direct-detection Dicke receiver is summarized and compared to previous published mm-wave imaging receivers in Table 3.

**TABLE 3.** Performance summary of the CDP-LNA-based dicke receiver and comparisons with state-of-the-art MM-wave imaging receivers.

| Ref. | [4] | [14] | [5] | [3] | [6] | [25] | **This Work** |
|---|---|---|---|---|---|---|---|
| Tech. | 0.18-µm SiGe | 0.13-µm SiGe | 0.12-µm SiGe | 65-nm CMOS | 65-nm CMOS | 65nm CMOS | **65-nm CMOS** |
| Integration | LNA RTPS PD BB | LNA PD | LNA SPDT PD | LNA Mixer PD BB | LNA SPDT PD | Switch LNA PD LPF | **LNA PD** |
| 3-dB BW (GHz) | 26 | 2.5 | 14 | 11 | 18 | - | **11.5** |
| NEP ($f$W/Hz$^{0.5}$) | 10 | 220 | 21 | 8.8 | 36 | 26 | **9.3** |
| NETD (K, 30ms) | 0.4 | 9# | 0.83 | 1 | 1.1 | 2.0 | **0.65** |
| Responsivity (MV/W) | 43 | 0.8 | 5 | 16 | 0.67 | 1.2 | **2.5** |
| Power (mW) | 200 | 11.7 | 34.8 | 101.6 | 110 | 152 | **52.6** |
| Area (mm$^2$) | 12.5 | 0.51 | 0.4 | 3 | 0.4 | 0.55 | **0.5** |

#Integration time of 1s; PD = power detector; BB = baseband; LPF = low pass filter

## V. CONCLUSION

A switch-less direct-detection Dicke receiver was implemented based on a CDP-LNA in a 65-nn CMOS technology. By using negative transformer feedback and inductive feedback techniques, the CDP-LNA exhibits power gain of 26.8 dB and 3-dB bandwidth of 25.5 GHz. With a power consumption of 52.6 mW, the CDP-LAN based direct-detection Dicke receiver achieves 9.3 $f$W/Hz$^{0.5}$ NEP, 0.65 K NETD, and 2.5 MV/W peak, responsivity. The proposed wideband CDP-LNA presents high gain, wide bandwidth, and high isolation between two paths without any insertion loss. Although it is used for the implementation of switch-less Dicke receiver for imaging applications, it can also be adopted for multi-antenna communication systems with different polarizations or frequencies.

## ACKNOWLEDGMENT

The authors would like to thank Mr. K. Yang, Mr. Z. Liang, and Mr. C. Li in VIRTUS, IC Design Center of Excellence, Nanyang Technological University, for supporting the chip measurement.

## REFERENCES

[1] A. Tang, Q. J. Gu, and M. C. F. Chang, "CMOS receivers for active and passive mm-wave imaging," *IEEE Commun. Mag.*, vol. 49, no. 10, pp. 190–198, Oct. 2011.
[2] L. Yujiri, M. Shoucri, and P. Moffa, "Passive millimeter wave imaging," *IEEE Microw. Mag.*, vol. 4, no. 3, pp. 39–50, Sep. 2003.
[3] L. Zhou, C.-C. Wang, Z. Chen, and P. Heydari, "A W-band CMOS receiver chipset for millimeter-wave radiometer systems," *IEEE J. Solid-State Circuits*, vol. 46, no. 2, pp. 378–391, Feb. 2011.
[4] L. Gilreath, V. Jain, and P. Heydari, "Design and analysis of a W-band SiGe direct-detection-based passive imaging receiver," *IEEE J. Solid-State Circuits*, vol. 46, no. 10, pp. 2240–2252, Oct. 2011.
[5] J. W. May and G. M. Rebeiz, "Design and characterization of *W*-Band SiGe RFICs for passive millimeter-wave imaging," *IEEE Trans. Microw. Theory Techn.*, vol. 58, no. 5, pp. 1420–1430, May 2010.
[6] A. Tomkins, P. Garcia, and S. P. Voinigescu, "A passive W-band imaging receiver in 65-nm bulk CMOS," *IEEE J. Solid-State Circuits*, vol. 45, no. 10, pp. 1981–1991, Oct. 2010.
[7] G. Feng, C. C. Boon, F. Meng, and X. Yi, "A 100-GHz 0.21-K NETD 0.9-mW/pixel charge-accumulation super-regenerative receiver in 65-nm CMOS," *IEEE Microw. Wireless Compon. Lett.*, vol. 26, no. 7, pp. 531–533, Jul. 2016.
[8] D. Liu, *Advanced Millimeter-wave Technologies: Antennas, Packaging and Circuits*. Hoboken, NJ, USA: Wiley, 2009.
[9] F. Sizov and A. Rogalski, "THz detectors," *Prog. Quantum Electron.*, vol. 34, no. 5, pp. 278–347, 2010.
[10] J. J. Lynch *et al.*, "Passive millimeter-wave imaging module with preamplified zero-bias detection," *IEEE Trans. Microw. Theory Techn.*, vol. 56, no. 7, pp. 1592–1600, Jul. 2008.
[11] R. Dicke, "The measurement of thermal radiation at microwave frequencies," *Rev. Sci. Instrum.*, vol. 17, no. 7, pp. 268–275, 1946.
[12] F. Meng, K. Ma, and K. S. Yeo, "A 130-to-180GHz 0.0035mm$^2$ SPDT switch with 3.3dB loss and 23.7dB isolation in 65nm bulk CMOS," in *IEEE Int. Solid-State Circuits Conf. (ISSCC) Dig. Tech. Papers*, Feb. 2015, pp. 1–3.
[13] F. Meng, K. Ma, K. S. Yeo, C. C. Boon, W. M. Lim, and S. Xu, "A 220–285 GHz SPDT switch in 65-nm CMOS using switchable resonator concept," *IEEE Trans. THz Sci. Technol.*, vol. 5, no. 4, pp. 649–651, Jul. 2015.
[14] L. Aluigi, D. Pepe, F. Alimenti, D. Zito, "K-band SiGe system-on-chip radiometric receiver for remote sensing of the atmosphere," *IEEE Trans. Circuits Syst. I, Reg. Papers*, vol. 64, no. 12, pp. 3025–3035, Dec. 2017.
[15] T. Yao *et al.*, "Algorithmic design of CMOS LNAs and PAs for 60-GHz radio," *IEEE J. Solid-State Circuits*, vol. 42, no. 5, pp. 1044–1057, May 2007.
[16] G. Feng, C. C. Boon, F. Meng, X. Yi, and C. Li, "An 88.5–110 GHz CMOS low-noise amplifier for millimeter-wave imaging applications," *IEEE Microw. Wireless Compon. Lett.*, vol. 26, no. 2, pp. 134–136, Feb. 2016.
[17] A. V. Oppenheim, A. S. Willsky, and S. H. Nawab, *Signals and Systems*. Upper Saddle River, NJ, USA: Prentice-Hall, 1997, pp. 674–683.
[18] G. Feng *et al.*, "Pole-converging intrastage bandwidth extension technique for wideband amplifiers," *IEEE J. Solid-State Circuits*, vol. 52, no. 3, pp. 769–780, Mar. 2017.
[19] X. Li, S. Shekhar, and D. J. Allstot, "G$_m$-boosted common-gate LNA and differential colpitts VCO/QVCO in 0.18$\mu$m CMOS," *IEEE J. Solid-State Circuits*, vol. 40, no. 12, pp. 2609–2619, Dec. 2005.
[20] H. G. Han, D. H. Jung, and T. W. Kim, "A 2.88 mW + 9.06 dBm IIP3 common-gate LNA with dual cross-coupled capacitive feedback," *IEEE Trans. Microw. Theory Techn.*, vol. 63, no. 3, pp. 1019–1025, Mar. 2015.
[21] A. Ç. Ulusoy *et al.*, "A SiGe D-band low-noise amplifier utilizing gain-boosting technique," *IEEE Microw. Wireless Compon. Lett.*, vol. 25, no. 1, pp. 61–63, Jan. 2015.
[22] B. Cetinoneri, Y. A. Atesal, A. Fung, and G. M. Rebeiz, "*W*-band amplifiers with 6-dB noise figure and milliwatt-level 170–200-GHz doublers in 45-nm CMOS," *IEEE Trans. Microw. Theory Techn.*, vol. 60, no. 3, pp. 692–701, Mar. 2012.
[23] D. Fritsche, G. Tretter, C. Carta, and F. Ellinger, "Millimeter-wave low-noise amplifier design in 28-nm low-power digital CMOS," *IEEE Trans. Microw. Theory Techn.*, vol. 63, no. 6, pp. 1910–1922, Jun. 2015.
[24] D. Sandstrom, M. Varonen, M. Karkkainen, and K. Halonen, "W-band CMOS amplifiers achieving +10dBm saturated output oower and 7.5dB NF," in *IEEE Int. Solid-State Circuits Conf. (ISSCC) Dig. Tech. Papers*, Feb. 2009, pp. 486–487,487a.
[25] Q. J. Gu, Z. Xu, A. Tang, and M. Chang, "A D-band passive imager in 65 nm CMOS," *IEEE Microw. Wireless Compon. Lett.*, vol. 22, no. 5, pp. 263–265, May 2012.

**GUANGYIN FENG** (S'12–M'16) received the B.Eng. degree from Northeastern University, China, in 2010, and the Ph.D. degree from Nanyang Technological University, Singapore, in 2016. Since 2016, he has been with Nanyang Technological University as a Research Fellow. His research interests include mm-wave/terahertz-integrated circuits and systems for imaging and wireless communications.

Dr. Feng serves as a reviewer for several IEEE journals and conferences.

**XIANG YI** (S'11–M'13) received the B.E. degree from the Huazhong University of Science and Technology in 2006, the M.S. degree from the South China University of Technology in 2009, and the Ph.D. degree from Nanyang Technological University (NTU) in 2014. He was a Research Fellow with NTU from 2014 to 2017. He is currently a Post-Doctoral Fellow with the Massachusetts Institute of Technology. His research interests include radio frequency, millimeter-wave, and terahertz-frequency synthesizers and transceiver systems.

Dr. Yi was a recipient of the IEEE ISSCC Silkroad Award and the SSCS Travel Grant Award in 2013. He is a technical reviewer for several IEEE journals and conferences.

**FANYI MENG** (S'11–M'16) received the B.Eng. and Ph.D. degrees in electrical and electronic engineering from Nanyang Technological University (NTU), Singapore, in 2011 and 2016, respectively. He joined NTU as a Research Fellow in 2015, where he served as the Co-Principal Investigator for several research projects. He is currently an Associate Professor with the University of Electronic Science and Technology of China. His research interests include radio frequency, millimeter-wave, and terahertz integrated circuit and systems.

Dr. Meng was a recipient of IEEE Solid-State Circuits Society Student Travel Grant Award in 2015. He serves as a reviewer and a technical program committee member for several IEEE journals and conferences.

**CHIRN CHYE BOON** (M'09–SM'10) received the B.E. (Hons.) and Ph.D. degrees in electrical engineering from Nanyang Technological University (NTU), Singapore, in 2000 and 2004, respectively. Since 2005, he has been with NTU, where he is currently an Associate Professor. He was a Senior Engineer with Advanced RFIC. He specializes in the areas of radio frequency (RF) and mm-wave circuits and systems design for biomedical and communications applications. He has conceptualized, designed, and silicon-verified 80 circuits/chips for biomedical and communication applications. He has authored over 100 refereed publications in the fields of RF and mm-wave. He has authored the book *Design of CMOS RF Integrated Circuits and Systems* (World Scientific Publishing).

Dr. Boon serves as a committee member for various conferences. Since 2010, he has been the Program Director for RF and mm-wave research with the S$50 million Research Centre of Excellence, VIRTUS, NTU. He is the Principal Investigator for industry/government research grants of S$8 646 178.22. He was a recipient of the Year-2 Teaching Excellence Award and Commendation Award for Excellent Teaching Performance from the School of Electrical and Electronic Engineering, NTU. He is an Associate Editor for the IEEE TRANSACTIONS ON VERY LARGE SCALE INTEGRATION SYSTEMS and the Golden Reviewer of the *IEEE Electron Devices Letters*.